



A Comprehensive Model of Morphologically Realistic Cosmic Dust Particles: An Application to Mimic the Unusual Polarization Properties of the Interstellar Comet 2I/Borisov

Prithish Halder and Sujan Sengupta

Indian Institute of Astrophysics, Koramangala 2nd block, Bengaluru, Karnataka 560034, India; prithishh3@gmail.com, prithish.halder@iiap.res.in

Received 2022 December 10; revised 2023 February 24; accepted 2023 February 25; published 2023 April 10

Abstract

The cosmic dust particles found in space are mainly porous aggregates of smaller grains. Theoretically, these aggregates are replicated using fractal geometry, assuming a cluster of spheres. Although the light scattering response of cosmic dust aggregates has been thoroughly studied using clusters of spherical grains in the past few decades, the effect of irregularities on the surface of each grain in an entire aggregate has mostly been neglected. We introduce, for the first time, a visually realistic cosmic dust model that incorporates a mixture of rough fractal aggregates (RFA) and agglomerated debris (Solids) to replicate the unusual polarization–phase curve observed in the case of the interstellar comet 2I/Borisov at multiple wavelengths. The authenticity of the RFA structures has been verified by replicating light scattering results of circumstellar dust analogs from the Granada Amsterdam Light Scattering Database. We demonstrate that the light scattering response from the RFA structures has a very close resemblance to the experimental values. Finally, we model the observed polarization–phase curve of the interstellar comet 2I/Borisov using a mixture of RFA and solid particles. The best-fit data indicate the presence of a higher percentage of porous RFA structures (80%) owing to the fact that the comet carries a higher percentage of small and highly porous pristine cosmic dust particles. Further, the model indicates that the unusually steep polarimetric slope and the high dust-to-gas ratio in newer comets are mainly due to a higher porous-to-compact ratio.

Unified Astronomy Thesaurus concepts: Comets (280); Interstellar objects (52); Coma dust (2159); Polarimetry (1278); Radiative transfer simulations (1967)

1. Introduction

The subject of interstellar comets is a very recent development in the field of astronomy, which started to emerge after the discovery of the Oort cloud. It was Sen & Rana (1993) who first predicted that one should detect an interstellar comet once in 200 years. The discovery of the interstellar comet 2I/Borisov in 2019, by Gennady Borisov after 180 years of cometary research, has proved the above prediction to be true. Similar to other solar system comets, 2I/Borisov exhibited a distinct coma, allowing various researchers to study the physics and chemistry of the material content using spectroscopic and polarimetric observations. The spectroscopic studies of the comet 2I/Borisov indicate a dust-to-gas ratio similar to those observed in carbon-depleted comets of the solar system (Aravind et al. 2021; Yang et al. 2021). On the other hand, polarimetric observations indicate an unusually steep slope (Bagnulo et al. 2021). Generally, solar system comets are categorized into two polarimetric classes: low- and high-polarization comets depending on the dust-to-gas ratio observed in the coma (Chernova et al. 1993; Levasseur-Regourd et al. 1996). Apart from these two classes there exists a third class (Hadamcik & Levasseur-Regourd 2003) that has polarization higher than that of high-polarization comets, which has been observed only in the case one solar system comet, C/1995 O1 (Hale-Bopp). Such high polarization is believed to be due to the presence

of extremely small Rayleigh-size dust particles. The presence of Rayleigh-size dust particles in Hale-Bopp can be traced back to its origin in the outer regions of our solar system, where the physical environment is comparable to that of the interstellar medium. Similarly, 2I/Borisov is believed to have originated from the outer regions of its host stellar system. Although Hale-Bopp might have visited the Sun once before its last apparition, 2I/Borisov had not encountered any star before passing close to the Sun, and thus the comet may hold a huge population of pristine cosmic dust particles.

The interpretation and analysis of astronomical observations of dust in comets is mainly based on our knowledge of light scattering by morphologically irregular particles. The significance of dust particles having size comparable to the wavelength of incident light has been widely acknowledged (A’Hearn et al. 1995, 2011; Kimura et al. 2006; Zubko et al. 2006, 2020; Das et al. 2008; Kolokolova et al. 2015; Deb Roy et al. 2017; Halder et al. 2018; Halder & Ganesh 2021). The cosmic dust particles found in space are mainly porous fractal aggregates of smaller grains formed due to coagulation and ballistic agglomeration in the circumstellar or interstellar environment. Theoretically, these aggregates are replicated using fractal geometry, assuming a cluster of spherical grains. But the studies of modeling of the third class of comets (Hale-Bopp) done by Lasue & Levasseur-Regourd (2006), Lasue et al. (2009), and Markkanen et al. (2015) used aggregates of nonspherical monomers/grains and kept the monomer size fixed for multiple wavelengths. In order to verify whether 2I/Borisov holds a relatively large number of pristine cosmic dust particles or to have an estimate of the amount of pristine dust present in the coma of the comet, it is necessary to conduct



Original content from this work may be used under the terms of the [Creative Commons Attribution 4.0 licence](https://creativecommons.org/licenses/by/4.0/). Any further distribution of this work must maintain attribution to the author(s) and the title of the work, journal citation and DOI.

light scattering simulations over modeled pristine cosmic dust aggregates and replicate the observed unusual polarization with an exact computer-modeled replica of cosmic dust. The dust particles studied by the Rosetta/MIDAS and Rosetta/COSIMA suggest the presence of porous aggregated dust particles that resemble the morphology of interplanetary dust particles (IDPs; Schulz et al. 2015; Bentley et al. 2016; Güttler et al. 2019; Mannel et al. 2019). The IDPs collected from the Earth's stratosphere and Antarctic ice have irregular geometry, fluffy aggregates, and a fractal nature that represents the physical morphology of solar system cosmic dust (Brownlee 2003; Noguchi et al. 2015). Again, due to flash heating in the upper atmosphere, these IDP samples may not purely represent pristine cosmic dust. The cosmic dust analog aggregates prepared in the Granada Amsterdam Light Scattering facility using condensation flow apparatus represent the most pristine morphology of cosmic dust and are devoid of flash heating. The microgravity and laboratory experiments of dust–dust interactions conducted to replicate the conditions prevailing in the early solar system suggest the formation of a fractal assemblage of dust via ballistic agglomeration (Wurm & Blum 1998; Blum & Wurm 2000; Krause & Blum 2004). In a similar way, small dust particles in the interstellar medium may coagulate in the vicinity of dense molecular clouds. Hence, astronomers around the world use fractal aggregates/clusters of spheres to study the physical and/or optical properties of cosmic dust. Numerically, fractal aggregates are prepared using ballistic agglomeration techniques. These agglomeration techniques hold the physics behind the dust coagulation in circumstellar and protoplanetary disks, but the morphology of each grain in an aggregate lacks surface roughness or irregularities. Roughness has been a matter of concern for a longer period of time, and hence dust structures such as Gaussian random spheres, agglomerated debris, and rough spheroids have been developed by various researchers (Muinonen et al. 1996; Zubko et al. 2006; Kolokolova et al. 2015) to include the contribution of irregularities or roughness. Although these rough or irregular structures explain the contribution of roughness in the case of single particles and debris particles, the contribution of roughness or irregularities on the surface of each grain of a fractal aggregate remains unknown.

In the present investigation, for the first time, we use a visually realistic cosmic dust model, which is represented by a mixture of highly porous rough fractal aggregates (RFA; Halder 2022) and low-porosity Solids (agglomerated debris) to model the unusual polarization properties of the interstellar comet 2I/Borisov. The highly porous RFA structures, which are aggregates of irregular/rough grains, have a very close resemblance to the IDPs collected from Earth's stratosphere. Initially, the RFA-modeled dust particles are validated by replicating light scattering results from Granada Amsterdam Light Scattering Database for the different aggregate samples (1–6; Volten et al. 2007) of circumstellar or cosmic dust analogs (Rietmeijer et al. 1999; Nuth et al. 2000). Then, we model the observed polarization–phase curve and the polarimetric spectral gradient of the interstellar comet 2I/Borisov using a mixture of RFA model structures (high porosity) and Solids (low porosity) at the three wavelengths $\lambda = 0.557 \mu\text{m}$ (V_f filter), $0.655 \mu\text{m}$ (R_f filter), and $0.768 \mu\text{m}$ (I_f filter). Finally, we compare the observed dust-to-gas ratio with the intrinsic dust parameter, the porous-to-compact ratio, for the extremely high-polarization comets (2I/Borisov and Hale-Bopp) and low-

polarization comets (67P/C-G and 1P/Halley) to understand the dependence of dust-to-gas ratio on the intrinsic dust parameters.

2. Modeling Methodology

In this section, we describe the techniques employed to generate RFA and Solid particles used to replicate the light scattering results from the Granada Amsterdam Light Scattering Database and to model the polarization properties of the interstellar comet 2I/Borisov. The light scattering technique and the related light scattering parameters are also discussed in this section.

2.1. Fractal Aggregates

Fractal aggregates (FA) having polydisperse spheres are created following the BPCA and BCCA agglomeration techniques using the Java package FLAGE¹ (Skorupski et al. 2014). The structure of the FA is loaded in the package REST (Rough Ellipsoid Structure Tools;² Halder 2022) where the x , y , and z coordinates and radius of each sphere of an aggregate are scaled into an equivolume sphere made up of unit dipoles/lattice points. In REST the RFA algorithm removes those dipoles/lattice points that do not fall within the radius of each sphere and hence forms the resultant structure, which is a fractal aggregate of spheres but made up of dipoles/lattice points as shown in Figure 1(a). REST is a structural tool that generates realistic cosmic dust particles from spheres, super-ellipsoids and FA. FLAGE is a very useful Java tool to create aggregates of spherical grains. It takes the following physical parameters as input to create a proper fractal aggregate:

1. Number of spheres (N).
2. Radius of each sphere/primary particle (r_p).
3. Radius of aggregate ($R_a = \sqrt{5/3} R_g$, where R_a is the characteristic radius of the aggregate and R_g is the radius of gyration, which is defined in Equation (1)).
4. Fractal dimension (D_f , a dimensionality constant that characterizes a fractal structure and is defined by Equation (1)).
5. Fractal prefactor (k_f , a proportionality constant that is a prefactor of the fractal scaling relation defined by Equation (1)).
6. Porosity (the degree or percentage of space present within a fractal aggregate).
7. Aggregate type:
 - (a) ballistic particle cluster agglomeration (BPCA).
 - (b) ballistic cluster–cluster agglomeration (BCCA).
 - (c) diffusion-limited agglomeration (DLA).
 - (d) reaction-limited agglomeration (RLA).

The structural arrangement of an aggregate having N monodisperse (spheres having same size) spherical grains (each having radius r) is defined by the following equation (Sorensen et al. 1992):

$$N = k_f \left(\frac{R_g}{r} \right)^{D_f}. \quad (1)$$

But the aggregates found in space are polydisperse (spheres having different sizes) in nature. An aggregate having

¹ FLAGE <https://scattering.eu/>

² Rough Ellipsoid Structure Tools (REST) <https://rest-package.readthedocs.io/>.

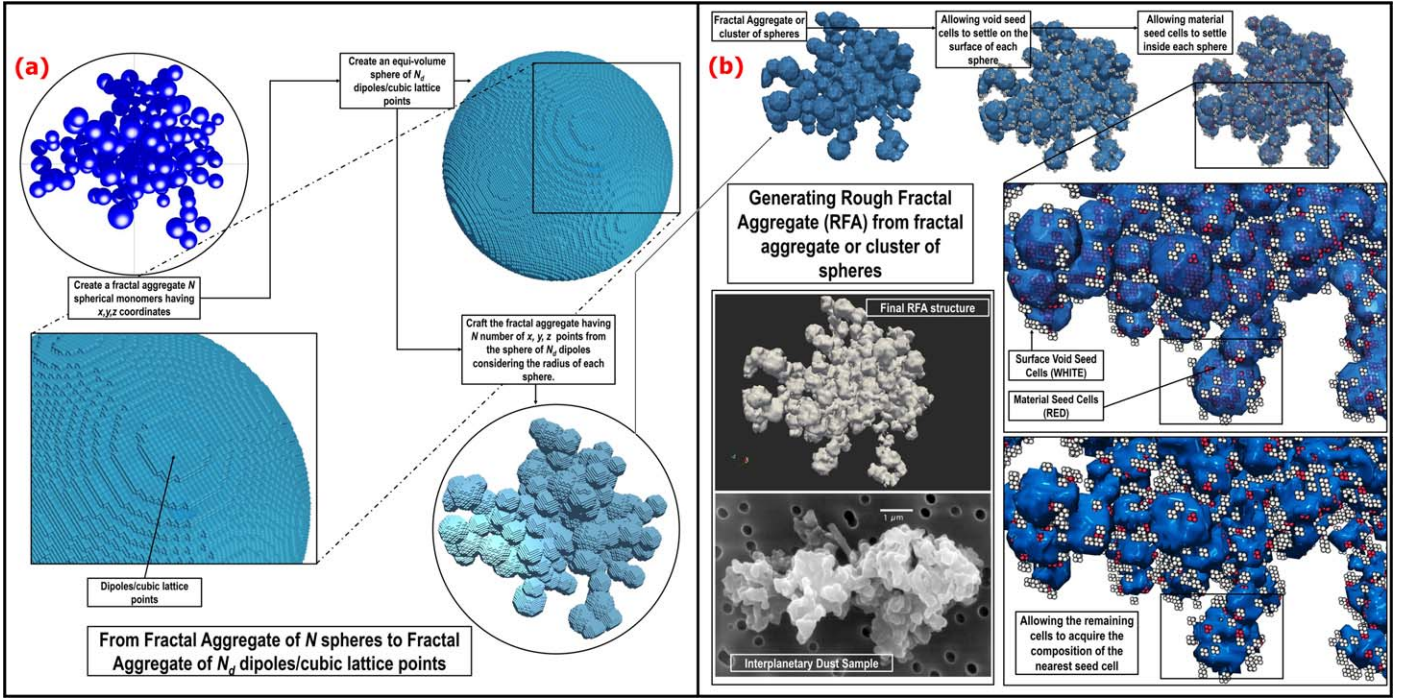


Figure 1. (a) Algorithm to generate fractal aggregates having N_d dipoles and (b) algorithm to generate rough fractal aggregates using REST (Halder 2022).

polydisperse spherical grains with primary particle (PP) radius r_p , average PP mass \overline{m}_p , and aggregate mass m_a is defined by Eggersdorfer & Pratsinis (2011) as

$$\frac{m_a}{\overline{m}_p} = k_f \left(\frac{R_g}{r_p} \right)^{D_f}, \quad (2)$$

where $m_a/\overline{m}_p = N$ is the number of PPs in the aggregate.

The fractal dimension is directly related to the porosity of an aggregate. The BCCA aggregates have porosity $\geq 95\%$ and $D_f < 2$, while the BPCA aggregates have porosity $\leq 90\%$ and $D_f > 2$. The porosity of different FA structures is controlled by changing $D_f = 1.8-2.5$. This is done to incorporate minute variation in porosity following the explanations provided for the different aggregate samples from the Granada Amsterdam Light Scattering Database. The aggregate samples 1 and 2 (Volten et al. 2007) are made up of the same material, with the same grain size and the same aggregate size, yet the polarization maximum (P_{\max}) for the two samples is different. It is already clear from previous studies that a slight increase in porosity will induce an increase in the P_{\max} value (Kimura et al. 2006; Halder et al. 2018). Also, the authors of the Granada Amsterdam Light Scattering Database have mentioned that this shift in P_{\max} for the aggregate samples 1 and 2 is possibly due to a minute difference in porosity.

2.2. Rough Fractal Aggregates

The RFA structures used in this study are generated using the Java package REST (Halder 2022) from the loaded FA structure file. The RFA algorithm in REST crafts surface roughness/irregularities on the surface of each spherical grain of an FA structure (see Figure 1(b)). The algorithm to generate the RFA structures is given below:

1. Browse and select the structure file of a fractal aggregate/cluster of spheres having the following format ($i, R, X Y Z, mtag, mtag$), where i is the sphere number, R is the radius of the i th sphere (in μm), X, Y, Z are the coordinates of each sphere (monomer), and $mtag$ is the composition tag.
2. Multiply each coordinate and radius by an integer scale factor n . This done to achieve the desired number of dipoles (N_d) for the entire RFA structure.
3. Measure the distance (d_{mono}) of each monomer from the center (0, 0, 0).
4. Create the initial sphere having N_d dipoles and radius $R_d = \text{maximum}(d_{\text{mono}})$ (in number of dipoles) from the center of the initial sphere.
5. Randomly choose N_{ss} surface seed cells on the surface of the FA inside the initial sphere.
6. Randomly choose N_m material seed cells inside the surface of the FA.
7. Measure the distance $D_m^{i,j}$ between the j th material seed cell and i th dipole of the base structure, where $j = 1$ to N_m and $i = 1$ to N_d .
8. Measure the distance $D_{ss}^{i,k}$ between the k th surface space seed cell and i th dipole of the base structure, where $k = 1$ to N_{ss} and $i = 1$ to N_d .
9. Print those dipoles for which $D_m^i < D_{ss}^i$ in the final RFA structure file.

The porosity P of a fractal aggregate is determined by the ratio of the total number of space seed cells in the entire volume of the sphere circumscribing the RFA structure to the total volume of the circumscribing sphere (Halder 2022),

$$\text{Volume of initial structure}(V_i) = N_d(\text{initial}) \times d^3$$

$$\text{Volume of final structure}(V_f) = N_d(\text{final}) \times d^3.$$

The total volume of space seed cells is given by

$$V_T = [N_d(\text{final}) - N_d(\text{initial})] \times d^3.$$

Therefore, the degree of porosity is

$$\begin{aligned} P &= \frac{V_T}{V_f} = \frac{[N_d(\text{final}) - N_d(\text{initial})] \times d^3}{N_d(\text{final}) \times d^3} \\ &= \frac{N_d(\text{final}) - N_d(\text{initial})}{N_d(\text{final})}. \end{aligned} \quad (3)$$

2.3. Generating Solid Structures

The Solid structures used in this study are low-porosity agglomerated debris particles generated using REST following the poked structure (PS) option/algorithm. The steps to generate PS shape are as follows:

1. Generate an initial spherical structure file `target.out` having N_d dipoles and radius R (in number of dipoles) using the `CALLTARGET` module.
2. Randomly choose N_m material seed cells from the N_d dipoles present in the `target.out` file.
3. Randomly choose N_{is} internal space seed cells from the N_d dipoles present in the `target.out` file.
4. Randomly choose N_{ss} surface space seed cells from the N_d dipoles present in the `target.out` file. The surface thickness should be t times r .
5. Measure the distance $D_m^{i,j}$ between the j th material seed cell and i th dipole of the base structure, where $j = 1$ to N_m and $i = 1$ to N_d .
6. Measure the distance $D_{is}^{i,k}$ between the k th internal space seed cell and i th dipole of the base structure, where $k = 1$ to N_{is} and $i = 1$ to N_d .
7. Measure the distance $D_{ss}^{i,l}$ between the l th surface space seed cell and i th dipole of the base structure, where $l = 1$ to N_{ss} and $i = 1$ to N_d .
8. Print those dipoles for which $D_m^i < D_{is}^i$ and $D_m^i < D_{ss}^i$ in the final structure file.

The steps to generate Solid structures (agglomerated debris particles) using the PS algorithm are:

1. R_d (in number of dipoles) = 64
2. $N_m = 21$
3. $N_{is} = 20$
4. $N_{ss} = 100$
5. $t = 1\%$

2.4. Light Scattering Simulations

The coma of a comet is optically thin and has a low volume concentration of dust particles. Hence, in theoretical modeling of the light scattering by the dust particles in the coma of a comet, multiple scattering effects are neglected. The scattering phenomenon for a mirror-symmetric and macroscopically isotropic particulate medium is defined by the scattering matrix, which represents far-field transformation of the Stokes parameters of the incident light (I_i, Q_i, U_i, V_i) to those of the scattered light (I_s, Q_s, U_s, V_s). This scattering matrix is given by

Bohren & Huffman (1998):

$$\begin{pmatrix} I_s \\ Q_s \\ U_s \\ V_s \end{pmatrix} = \frac{1}{k^2 d^2} \begin{pmatrix} S_{11} & S_{12} & 0 & 0 \\ S_{12} & S_{22} & 0 & 0 \\ 0 & 0 & S_{33} & S_{34} \\ 0 & 0 & -S_{34} & S_{44} \end{pmatrix} \begin{pmatrix} I_i \\ Q_i \\ U_i \\ V_i \end{pmatrix}, \quad (4)$$

where k is the wavenumber, d is the distance between the scatterer and the observer, and S_{ij} represents the orientationally symmetric scattering matrix elements. The angle α between the Sun, comet, and Earth is called the phase angle. Angle $\theta = 180^\circ - \alpha$ is called the scattering angle, $\theta = [0^\circ, 180^\circ]$.

In this work, we study the following light scattering parameters defined by the scattering matrix elements:

1. Phase function: S_{11}
2. Degree of linear polarization: $DP = -S_{12}/S_{11}$.
3. S_{22}/S_{21} .

The anisotropy condition for a nonspherical scatterer is $S_{11} \neq S_{22}$ and $S_{33} \neq S_{44}$.

We use the discrete dipole approximation scattering codes³ (Draine & Flatau 1994) in parallel mode for the numerical simulations of light scattering.

Further, the results are averaged using the power-law size distribution r^{-n} where n ranges between 2.0 and 3.0. The power-law size distribution is modeled by considering aggregates of different sizes from smallest to largest. The aggregate sizes are increased by increasing the number of monomers/grains and keeping the monomer size fixed.

2.5. Dust Model

In this study, we have considered two kinds of modeling approaches to extract the best possible results. The first modeling approach considers fixed values of monomer size parameters (x) for all the three wavelengths and we term it as Model _{x} . The second modeling approach considers fixed values of monomer size (r) for all the three wavelengths and we term it as Model _{r} . In both models we use a mixture of highly porous RFA structures and Solid agglomerated debris particles. As silicates and carbonaceous materials constitute the majority of the composition of dust found in comets (Bardyn et al. 2017), we have considered the refractive indices of amorphous forsterite to represent silicates and amorphous carbon to represent carbonaceous materials. Figure 2 shows the wavelength dependence of refractive index for both amorphous forsterite (Scott et al. 1996) and amorphous carbon (Jenniskens & Jenniskens 1993; Li et al. 1997), while the specific values of refractive indices in the three wavelengths for silicate and carbon are shown below.

$$\text{Silicate} \begin{cases} 1.68 + 0.0035i, & \text{for } \lambda = 0.557 \mu\text{m} \\ 1.67 + 0.0040i, & \text{for } \lambda = 0.655 \mu\text{m} \\ 1.66 + 0.0048i, & \text{for } \lambda = 0.768 \mu\text{m} \end{cases}$$

$$\text{Carbon} \begin{cases} 1.97 + 0.23i, & \text{for } \lambda = 0.557 \mu\text{m} \\ 1.99 + 0.22i, & \text{for } \lambda = 0.655 \mu\text{m} \\ 2.0 + 0.2i, & \text{for } \lambda = 0.768 \mu\text{m} \end{cases}.$$

³ Discrete dipole approximation DDSCAT version 7.3.3 <http://ddscat.wikidot.com/>

Table 1
Model_X RFA Parameters

N	X_a	D_f	$r_p(\lambda = 0.557 \mu\text{m})$	$R_a(\lambda = 0.557 \mu\text{m})$	$r_p(\lambda = 0.655 \mu\text{m})$	$R_a(\lambda = 0.655 \mu\text{m})$	$r_p(\lambda = 0.768 \mu\text{m})$	$R_a(\lambda = 0.768 \mu\text{m})$
45	5	1.8	0.062 μm	0.44 μm	0.073 μm	0.52 μm	0.085 μm	0.61 μm
625	21	1.8	0.062 μm	1.91 μm	0.073 μm	2.25 μm	0.085 μm	2.62 μm

Note. Details of different parameters of RFA structures such as number of monomers (N), aggregate size parameter (X_a), fractal dimension (D_f), monomer radius (r_p), and aggregate radius (R_a) in the three different wavelengths for the minimum and maximum sizes respectively.

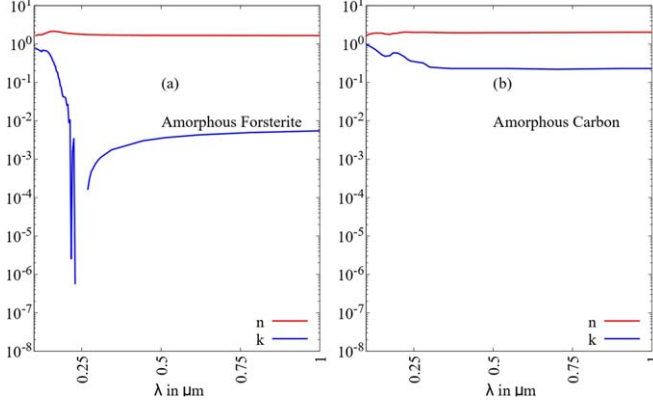


Figure 2. Variation of complex refractive index n (red line) and k (blue line) with increasing wavelength for (a) amorphous forsterite and (b) amorphous carbon.

The details of both the modeling approaches are explained in the following subsections.

2.5.1. Model_X: Constant Size Parameter

In this modeling approach we consider a fixed primary particle (monomer) size parameter ($x_p = 0.7$) for the RFA model structures, which corresponds to following PP (monomer) radii (r_p),

$$x_p = \frac{2\pi}{\lambda} r_p = 0.7 \begin{cases} r_p = 0.062 \mu\text{m}, & \text{for } \lambda = 0.557 \mu\text{m} \\ r_p = 0.073 \mu\text{m}, & \text{for } \lambda = 0.655 \mu\text{m} \\ r_p = 0.085 \mu\text{m}, & \text{for } \lambda = 0.768 \mu\text{m} \end{cases}.$$

The upper and lower size cutoffs of monomer size under Model_X are defined using a log-normal size distribution having standard deviation of $\sigma_p = \pm 0.03 \mu\text{m}$. Thus the smallest monomer sizes are 0.032 μm , 0.043 μm , and 0.055 μm at V_f , R_f , and I_f filters respectively. The largest monomer sizes are 0.092 μm , 0.103 μm , and 0.115 μm at V_f , R_f , and I_f filters respectively. In total, 50 RFA aggregates are considered having aggregate size parameters (X_a) in the range 5–20 and number of monomers (N) in the range 45–625 (see Table 1 for more details).

On the other hand, for the low-porosity solid particles we have considered agglomerated debris particles generated using REST. A total of 50 solid particles are considered having minimum size parameter 0.65 and maximum size parameter 20. The respective minimum and maximum radii of the solids for the three wavelengths are

$$X_{\min} = \frac{2\pi}{\lambda} R = 0.65 \begin{cases} R = 0.057 \mu\text{m}, & \text{for } \lambda = 0.557 \mu\text{m} \\ R = 0.067 \mu\text{m}, & \text{for } \lambda = 0.655 \mu\text{m} \\ R = 0.079 \mu\text{m}, & \text{for } \lambda = 0.768 \mu\text{m} \end{cases}$$

$$X_{\max} = \frac{2\pi}{\lambda} R = 20 \begin{cases} R = 1.77 \mu\text{m}, & \text{for } \lambda = 0.557 \mu\text{m} \\ R = 2.08 \mu\text{m}, & \text{for } \lambda = 0.655 \mu\text{m} \\ R = 2.44 \mu\text{m}, & \text{for } \lambda = 0.768 \mu\text{m} \end{cases}.$$

Tables 1 and 2 show all the details of different parameters used in Model_X.

2.5.2. Model_R: Constant Monomer Radius

In this modeling approach we consider fixed value of primary particle (monomer) radius or mean monomer radius $r_p = 0.073 \mu\text{m}$ for all the three wavelengths, while the aggregate radius (R_a) is considered to be in the range 0.22–2.0 μm for all the wavelengths (see Table 3 for more details). On the other hand the radius/size (R) of solid particles is also fixed for all the wavelengths. The minimum and maximum radii of PP (monomers) and the related size parameters for the three respective wavelengths are shown below:

$$r_p = \frac{\lambda}{2\pi} x_p = 0.073 \mu\text{m} \begin{cases} x_p = 0.82, & \text{for } \lambda = 0.557 \mu\text{m} \\ x_p = 0.70, & \text{for } \lambda = 0.655 \mu\text{m} \\ x_p = 0.60, & \text{for } \lambda = 0.768 \mu\text{m} \end{cases}.$$

The upper and lower size cutoffs of monomer size under Model_R are defined using a log-normal size distribution having a standard deviation of $\sigma_p = \pm 0.03 \mu\text{m}$. Thus the size of the smallest and the largest monomer in an aggregate are 0.043 μm and 0.103 μm for all the three wavelengths. For the low porous/low-porosity solid particles, 50 structures are generated in the size range 0.07–2.0 μm for all the wavelengths. The minimum and maximum radii of Solids and the related size parameters for the three respective wavelengths are shown below:

$$R_{\min} = \frac{\lambda}{2\pi} X = 0.07 \mu\text{m} \begin{cases} X = 0.79, & \text{for } \lambda = 0.557 \mu\text{m} \\ X = 0.67, & \text{for } \lambda = 0.655 \mu\text{m} \\ X = 0.57, & \text{for } \lambda = 0.768 \mu\text{m} \end{cases}$$

$$R_{\max} = \frac{\lambda}{2\pi} X = 2.0 \mu\text{m} \begin{cases} X = 22.5, & \text{for } \lambda = 0.557 \mu\text{m} \\ X = 19.2, & \text{for } \lambda = 0.655 \mu\text{m} \\ X = 16.4, & \text{for } \lambda = 0.768 \mu\text{m} \end{cases}.$$

Table 4 shows all the details of different parameters used in Model_R.

Table 2
Model_X Solid Parameters

X	ρ_f	$R(\lambda = 0.557 \mu\text{m})$	$R(\lambda = 0.655 \mu\text{m})$	$R(\lambda = 0.768 \mu\text{m})$
0.65	0.26	0.057 μm	0.067 μm	0.079 μm
20	0.27	1.77 μm	2.08 μm	2.44 μm

Note. Details of different parameters of solid structures such as size parameter (X), packing fraction (ρ_f), and radius (R) in the three different wavelengths for the minimum and maximum sizes respectively.

Table 3
Model_R RFA Parameters

N	D_f	r_p	R_a	N_d	$X_a(\lambda = 0.557 \mu\text{m})$	$X_a(\lambda = 0.655 \mu\text{m})$	$X_a(\lambda = 0.768 \mu\text{m})$
10	1.8	0.073 μm	0.22	1675	2.48	2.11	1.79
625	1.8	0.073 μm	2.00	90,780	22.5	19.18	16.36

Note. Details of different parameters of RFA structures such as number of monomers (N), fractal dimension (D_f), monomer radius (r_p), aggregate radius (R_a), and aggregate size parameter (X_a) in the three different wavelengths for the minimum and maximum sizes respectively.

Table 4
Model_R Solid Parameters

R_a	ρ_f	$X(\lambda = 0.557 \mu\text{m})$	$X(\lambda = 0.655 \mu\text{m})$	$X(\lambda = 0.768 \mu\text{m})$
0.07 μm	0.26	0.79	0.67	0.57
2.0 μm	0.27	22.5	19.2	16.4

Note. Details of different parameters of solid structures such as radius (R), packing fraction (ρ_f), and size parameter (X) in the three different wavelengths for the minimum and maximum sizes respectively.

Table 5
Physical Properties of RFA Model Structures (1–6)

Sample ^a	RFA Structures ^b	n^c and Color ^d	Porosity	Grain Radius	Aggregate Radius (R_a)	Average Number of Dipoles (N_d)
1	1.1, 1.2, 1.3	1.7 dark brown	91%–95%	0.05–0.12 μm	0.65 μm	25,896
2	2.1, 2.2	1.7 dark brown	93%–94%	0.05–0.12 μm	0.65 μm	24,500
3	3.1, 3.2, 3.3	1.6 light brown	94%–95%	0.03–0.05 μm	0.65 μm	25,423
4	4.1, 4.2, 4.3	1.6 light brown	93%–94%	0.03–0.05 μm	0.6 μm	18,809
5	5.1, 5.2, 5.3	1.8 black	97%–99%	0.015–0.06 μm	0.375 μm	3305
6	6.1, 6.2, 6.3	1.7 black	91%–96%	0.015–0.06 μm	0.6 μm	19,324

Notes.

^a The different samples of circumstellar dust analogs prepared in the Granada Amsterdam Light Scattering setup are described in Table 3 of Volten et al. (2007).

^b The different realizations of the RFA model structures are shown in Figure 12 in the Appendix.

^c For simplicity we considered the imaginary part of the refractive index $k = 0.0001$ for all the structures, as it was not detected in the experiments.

^d The color refers to the observed colors of different samples from the experiments.

3. Results

In this section, we discuss the results from light scattering simulations of RFA structures for the aggregate samples (1–6) from the Granada Amsterdam Light Scattering Database. Finally, we explain the RFA + Solid model results used to model the observed polarization from the comet 2I/Borisov.

3.1. Validating RFA Model Structures

To replicate the morphology of cosmic dust aggregates, we generate the polydisperse RFA model structures using the package REST (Halder 2022). REST takes the structure file of a polydisperse FA and crafts roughness and/or irregularities on the surface of each spherical grain of an FA structure, thereby

creating the most realistic computer-modeled cosmic dust analog, as shown in Figure 1. To proceed further, it is necessary to cross-check whether the RFA model structures are reliable enough to be considered as pristine cosmic dust candidates to model the observed polarization of the comet 2I/Borisov. Thus, to validate the RFA model structures light scattering simulations are performed for each of the RFA model structures using the discrete dipole approximation (DDSCAT) to extract the light scattering parameters S_{11} (phase function), $-S_{12}/S_{11}$ (degree of linear polarization), and the ratio S_{22}/S_{11} for the respective model structures, where S_{ij} are the orientationally symmetric scattering matrix elements. The simulations are performed considering similar values of monomer size, aggregate size, refractive index, and porosity to those provided in the Granada Amsterdam Light

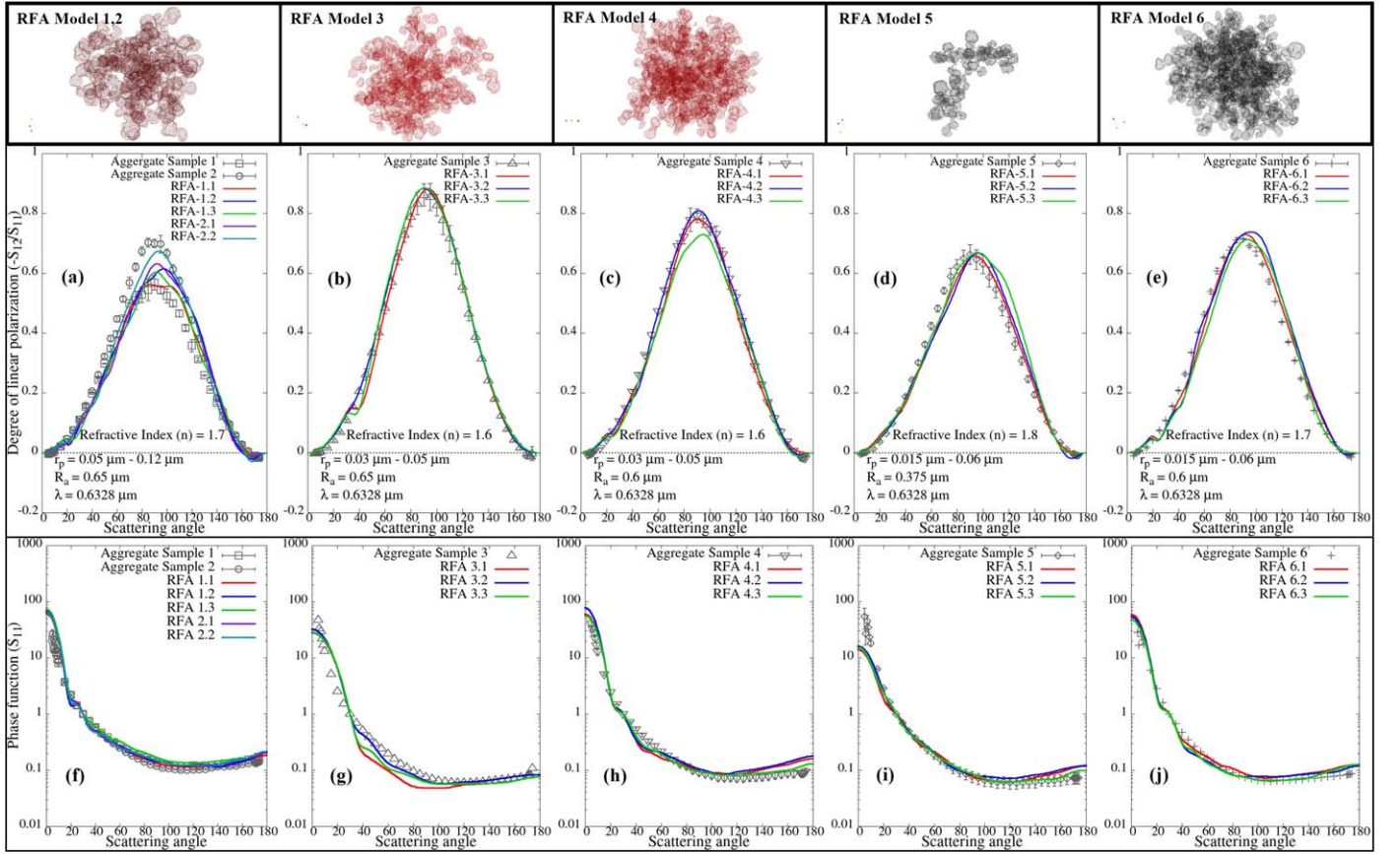


Figure 3. Variation of the degree of linear polarization $-S_{12}/S_{11}$ (a)–(e) and phase function S_{11} (f)–(j) with scattering angle for RFA model structures (1–6; solid lines) compared with the experimental results for aggregate samples (1–6; hollow squares and triangles) from the Granada Amsterdam Light Scattering Database (Volten et al. 2007).

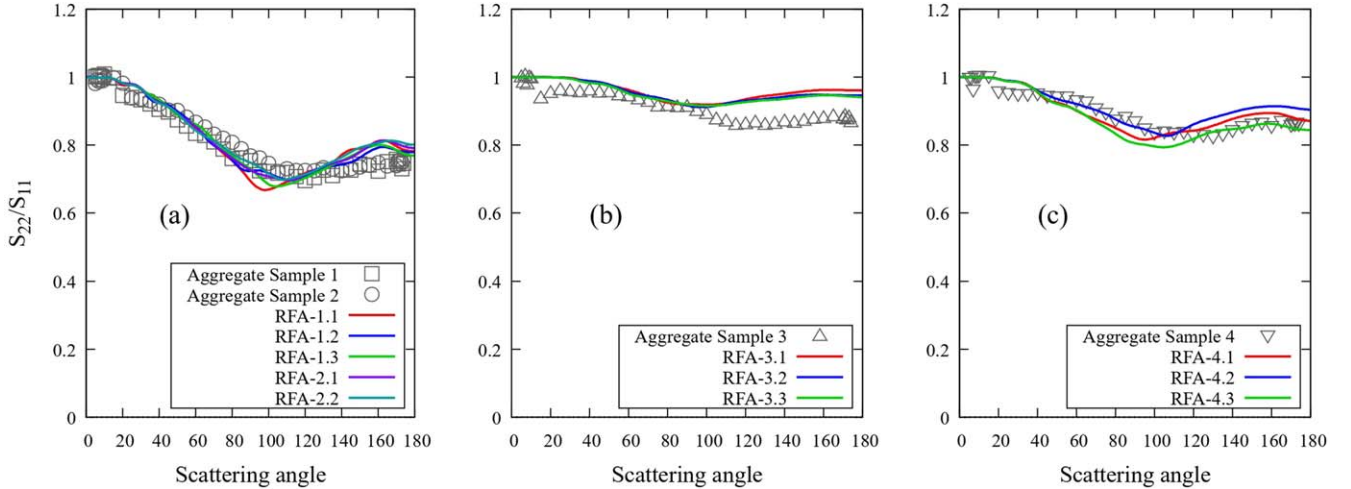


Figure 4. Variation of S_{22}/S_{11} (a)–(c) with scattering angle for RFA model structures (1–4; solid lines) compared with the experimental results for Aggregate Samples (1–4; hollow squares and triangles) from the Granada Amsterdam Light Scattering Database (Volten et al. 2007).

Scattering Database for the aggregate samples (1–6; see Table 5). Figure 3 shows the variation of $-S_{12}/S_{11}$ and S_{11} (normalized by $S_{11}(30^\circ)$ as in the case of experiments) with scattering angle for RFA model structures (1–6) compared with the experimental results for aggregate samples (1–6) from the Granada Amsterdam Light Scattering Database. Figure 4 shows the variation of S_{22}/S_{11} with scattering angle for RFA model structures (1–4) compared with those

obtained experimentally for aggregate samples (1–4). It is clear from the figures that when roughness is induced on the surface of spherical monomers of a fractal aggregate, a better agreement with the experimental data can be achieved. Hence, the RFA model structures not only look similar to original cosmic dust aggregates but can also produce light scattering responses similar to those obtained from light scattering experiments on cosmic dust analogs.

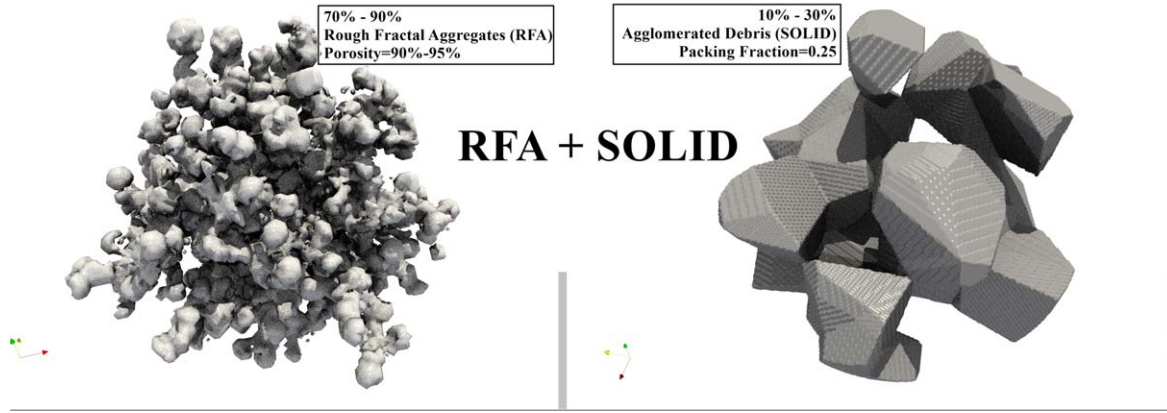


Figure 5. 3D visualization of RFA + Solid mixed morphology used to model the observed polarization–phase data of comet 2I/Borisov.

3.2. Modeling the Observed Polarization of 2I/Borisov

After validating the RFA model structures, we proceed further to develop a model of comet dust considering both porous cosmic dust aggregates (RFA) and low-porosity solid particles (Solids; see Figure 5). In this model, the RFA structures are considered to represent the porous cosmic dust aggregates, while the agglomerated debris particles are considered to represent low-porosity solid particles. The recent study on modeling of cometary polarization by Halder & Ganesh (2021) shows a detailed modeling technique where relatively larger particles are used to model both short- and long-period comets using hierarchical aggregates, fluffy solids, and agglomerated debris particles. Although the model is able to explain the observed polarization of short-period comets 1P/Halley, 67P/C-G (Halder & Ganesh 2021), and 156P/Russel-LINEAR (Aravind et al. 2022), it showed certain discrepancies in the negative polarization in the case of the comet Hale-Bopp. Thus, it is clear that the third class of comets requires a special treatment with a much simpler approach. Hence in the present study we consider smaller particles of size $\leq 2.5 \mu\text{m}$ with more pristine morphology.

We have used DDSCAT to compute the degree of linear polarization for the high-porosity RFA model structures and the low-porosity solid particles under the parameterization schemes of Model_X and Model_R discussed in Section 2.5. It is clear from the Rosetta/MIDAS findings that both high-porosity aggregates and low-porosity solids are present in a comet. Also, the carbon to silicate ratio or the ratio of highly absorbing material to less absorbing material was found to be 50:50. Initially we mixed the simulated polarization data of porous RFA structures for amorphous silicate and amorphous carbon at mixing ratios of C:Si = 60:40 and 50:50. Finally, we mixed the inhomogeneous RFA polarization data with Solid silicate data at mixing ratios of RFA:Solid = 80:20. The best-fit results obtained under both schemes are explained below.

3.2.1. Best-fit Results Using Model_X

Figure 6 depicts the variation in the degree of linear polarization using Model_X for RFA:Solid = 80:20 with varying power-law index n for the different wavelength filters $\lambda = 0.557 \mu\text{m}$ (V_f filter), $0.655 \mu\text{m}$ (R_f filter), and $0.768 \mu\text{m}$ (I_f filter) for C:Si = 50:50 (a)–(c) and C:Si = 60:40 (d)–(f). These figures portray a multidimensional approach of the model where we compare the observations of 2I/Borisov and Hale-Bopp for the particular power-law index at all three wavelengths. One can easily notice

from all the three figures that the polarimetric observations of the comets 2I/Borisov and Hale-Bopp show good agreement with model curves in the power-law index range of 2.4–2.8 at all three wavelengths, although the power-law index must remain consistent at all three wavelengths. This discrepancy may arise due to the consideration of fixed monomer size parameter, which is the basis of Model_X. This issue is resolved when fixed monomer size is considered at all three wavelengths as explained in the next section.

3.2.2. Best-fit Results Using Model_R

In the case of Model_X, the monomer size parameter is fixed for all three wavelengths, and the monomer radius is scaled according to the size parameter. But in a realistic case the monomer radius will remain constant for the smaller and larger aggregates at all wavelengths. This anomaly is corrected in Model_R, which considers a fixed value of monomer radius for all the aggregates at all three wavelengths. Hence, in this section, we study the variation of the degree of linear polarization and phase angle for changing aggregate sizes keeping the monomer radii fixed at all three wavelengths for silicate and carbon respectively for 50 RFA structures (see Figure 7) and 50 Solid particles following the parameterization scheme of Model_R explained in Section 2.5.2. Figure 8 depicts the variation in the degree of linear polarization using Model_R for RFA:Solid = 80:20 with varying power-law index n for the different wavelength filters $\lambda = 0.557 \mu\text{m}$ (V_f filter), $0.655 \mu\text{m}$ (R_f filter), and $0.768 \mu\text{m}$ (I_f filter) respectively for C:Si = 50:50 (a)–(c). It is clear from the figure that the best-fit size distribution index n remains consistent at 2.6, and this becomes clear from Figure 9, which shows the best-fit curves at $n = 2.6$ obtained using Model_R for the comet 2I/Borisov at the same three wavelengths for C:Si = 50:50.

3.3. Modeling the Polarimetric Spectral Gradient

In this section we discuss the observed and modeled polarimetric spectral gradient (PSG), which is defined by the following equation:

$$\frac{dP(\lambda)}{d\lambda} \simeq \text{PSG}_{(\lambda_1, \lambda_2)} = \frac{P(\lambda_2) - P(\lambda_1)}{\lambda_2 - \lambda_1}, \quad (5)$$

where P is the value of polarization (observed/modeled), while λ_1 and λ_2 are the two subsequent wavelengths. The polarimetric observations of the comet 2I/Borisov indicate that in the positive branch, polarization increases with increasing

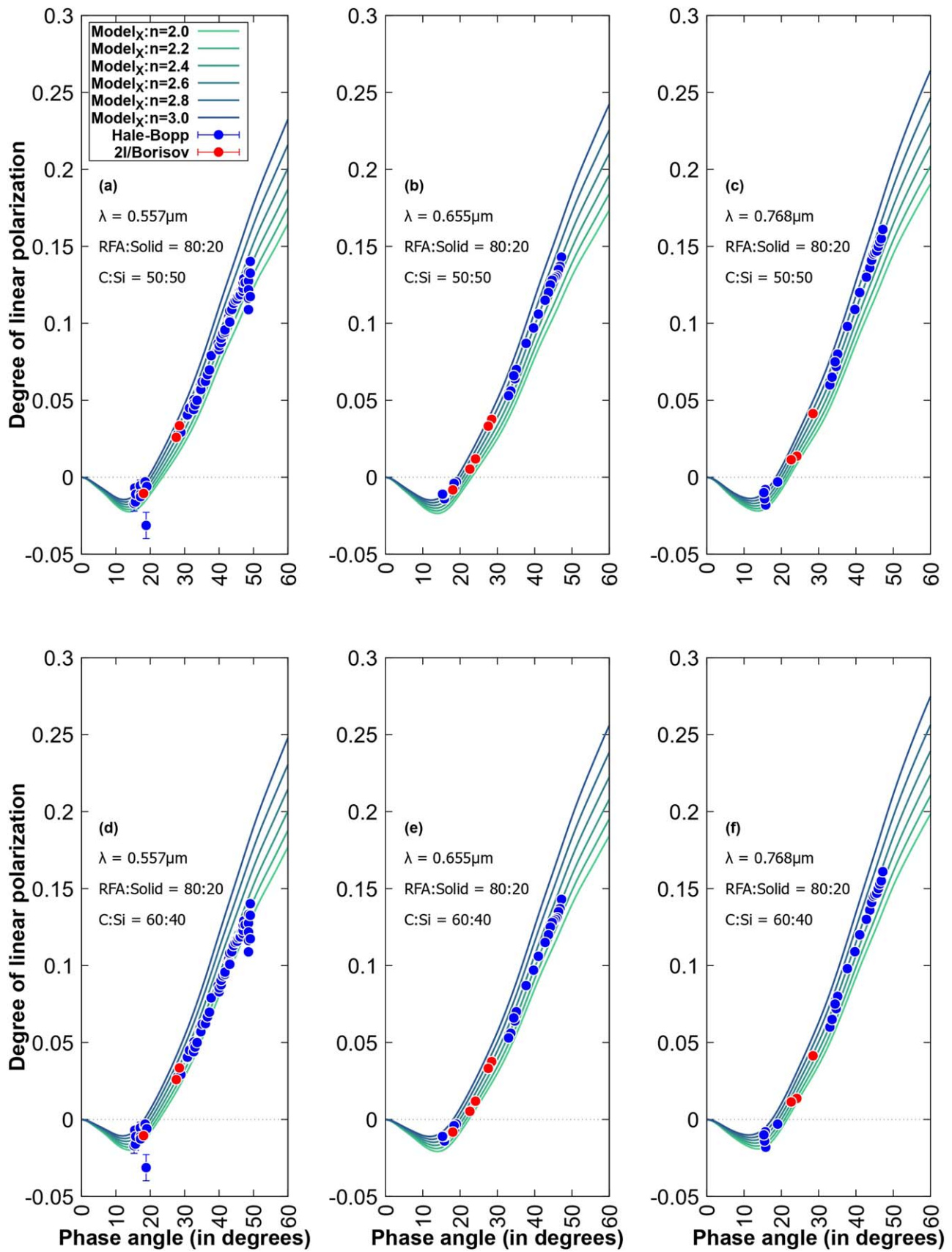


Figure 6. Variation of the degree of linear polarization with phase angle using Model_x for mixed morphology RFA:Solid = 80:20 over the power-law index range $n = 2.0$ – 3.0 having C:Si = 50:50 (a)–(c) and C:Si = 60:40 (d)–(f) for the wavelengths $\lambda = 0.557 \mu\text{m}$ (V_f filter), $0.655 \mu\text{m}$ (R_f filter), and $0.768 \mu\text{m}$ (I_f filter).

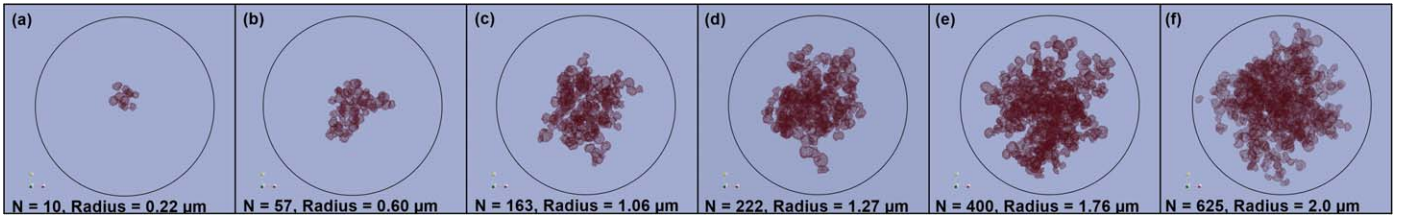


Figure 7. Visualization of six out of 50 RFA structures for Model_R having radii (a) $R_a = 0.22 \mu\text{m}$, (b) $R_a = 0.60 \mu\text{m}$, (c) $R_a = 1.06 \mu\text{m}$, (d) $R_a = 1.27 \mu\text{m}$, (e) $R_a = 1.76 \mu\text{m}$, and (f) $R_a = 2.0 \mu\text{m}$.

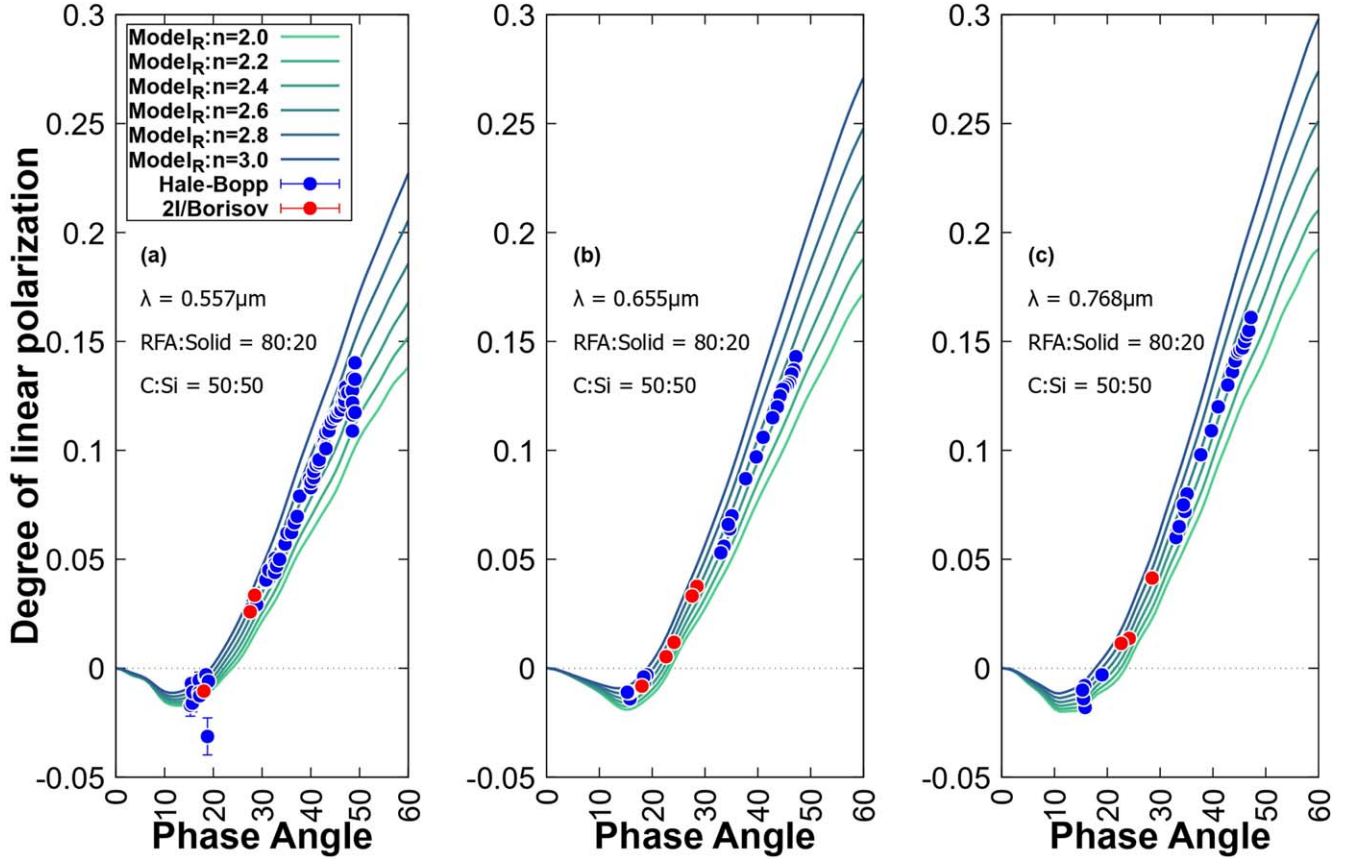


Figure 8. Variation of the degree of linear polarization with phase angle using Model_R for mixed morphology RFA:Solid = 80:20 over the power-law index range $n = 2.0$ – 3.0 having C:Si = 50:50 (a)–(c) for the wavelengths $\lambda = 0.557 \mu\text{m}$ (V_f filter), $0.655 \mu\text{m}$ (R_f filter), and $0.768 \mu\text{m}$ (I_f filter).

wavelength, and hence the PSG remains positive. The model PSG curves shown in Figure 10 under Model_X and Model_R indicate a similar trend, which is a common feature for all comets including the third class of comets that have a higher polarization than the high-polarization comets. But in the negative branch, the observed PSG becomes negative at phase angles around 20° for both Hale-Bopp and 2I/Borisov. Surprisingly, the modeled PSG also becomes negative around a phase angle of 20° . Although the model PSG(V_f , R_f) curve obtained using Model_X indicates a significant negative trend at low phase angles, it does not show a promising fit with the observed PSG points. Moreover, the model PSG(R_f , I_f) curve obtained using Model_X does not indicate any significant negative trend, which is observed in the case of Hale-Bopp. On the other hand, the model PSG(V_f , R_f) and PSG(R_f , I_f) obtained using Model_R show a significant negative trend at low phase angles, and also the model curves almost fit some of the

observed points and remain relatively close to others. Hence, Model_R, which considers a fixed value of monomer radius at all three wavelengths, produces better results, while Model_X, which considers a fixed monomer size parameter, is physically incorrect as is clear from the PSG plot.

3.4. Exploring the Relation between Dust-to-Gas Ratio and Intrinsic Dust Parameters

The best-fit model data for the observed polarization and PSG of the third class of comets, 2I/Borisov and Hale-Bopp, and those of short-period comets 1P/Halley and 67P/C-G, obtained from the light scattering simulations explained in this study and Halder & Ganesh (2021) respectively, indicate that the intrinsic properties of dust play a crucial role in defining the signature polarimetric slope of different classes of comets. For example, in this study the porous-to-compact ratio (RFA:Solid) obtained for the comets 2I/Borisov and Hale-Bopp (third class

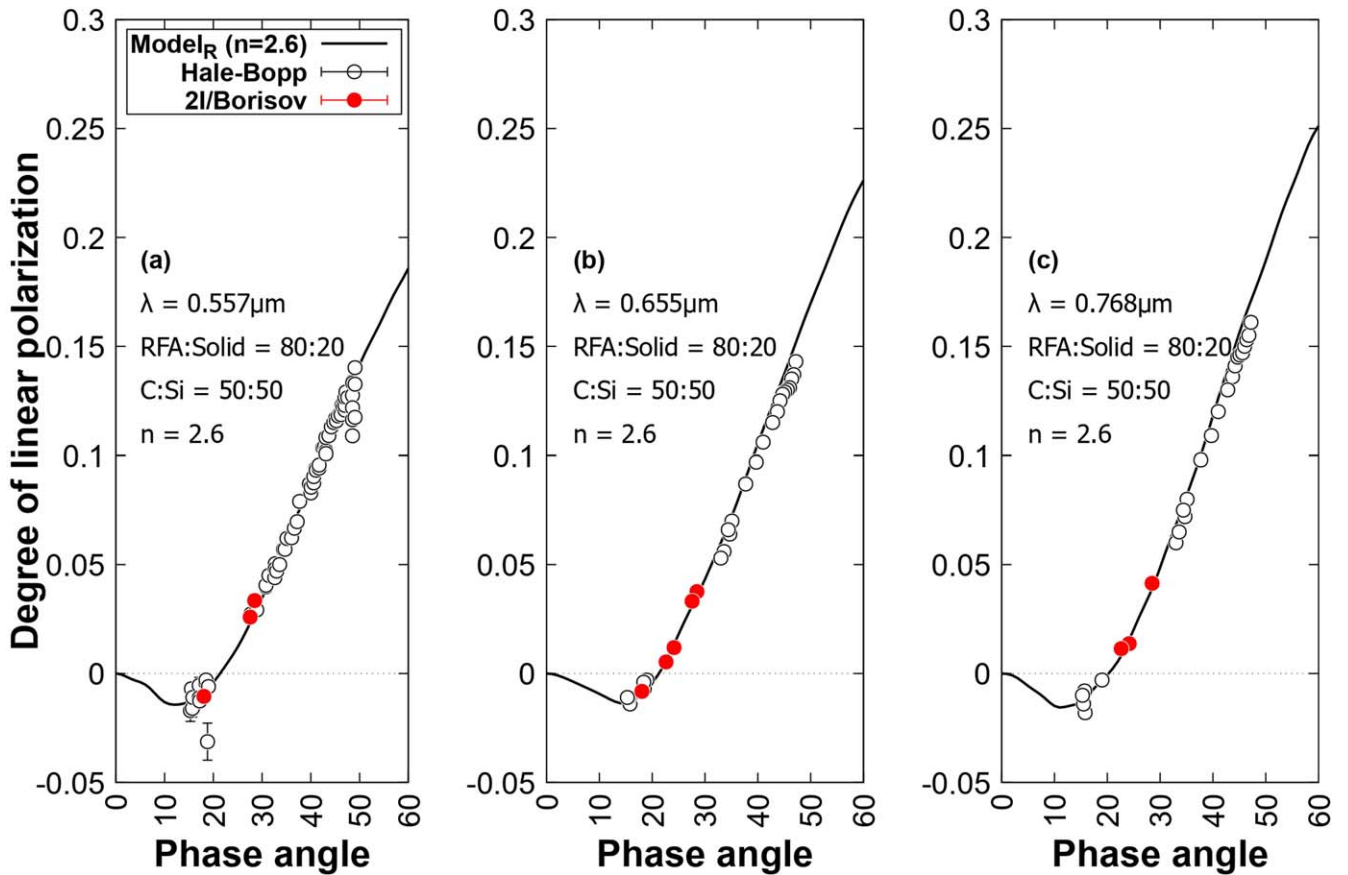


Figure 9. Best-fit model results using Model_R for the interstellar comet 2I/Borisov with the observations (red filled circles) at wavelengths $\lambda = 0.557 \mu\text{m}$ (V_f filter), $0.655 \mu\text{m}$ (R_f filter), and $0.768 \mu\text{m}$ (I_f filter) (a)–(c) and comparison with the polarimetric observations of the comet C/1995 O1 (Hale-Bopp) (white open circles) at $\lambda = 0.4845 \mu\text{m}$ (Ganesh et al. 1998), $0.620 \mu\text{m}$ (Ganesh et al. 1998), and $0.730 \mu\text{m}$ (Kikuchi 2006) for C:Si = 50:50 ($n = 2.6$).

of comets) is 4. While the porous-to-compact ratio (Hierarchical Aggregate:Solid) obtained for comets 1P/Halley and 67P/C-G (short-period comets) is 0.25. Thus, the difference in polarization or the polarimetric slope of different classes of comets tends to be proportional to the porous-to-compact ratio of dust in the coma of the comet. In a similar way, the dust-to-gas ratio in the coma of a comet is proportional to the polarization or polarimetric slope. Figure 11 depicts the respective dust-to-gas ratio and porous-to-compact ratio for the aforesaid comets. It is clear from the figure that high dust-to-gas ratio in the third class of comets is accompanied by a high porous-to-compact ratio of dust particles, while in low-polarization comets the dust-to-gas ratio is accompanied by a low porous-to-compact ratio.

4. Discussion

Under the framework of polarimetric observations of the interstellar comet 2I/Borisov (Bagnulo et al. 2021) and the light scattering experiments on different aggregate samples of cosmic dust analogs from the Granada Amsterdam Light Scattering Database (Volten et al. 2007) we develop a visually realistic dust model to replicate the unusual polarization–phase curve observed in the comet 2I/Borisov. We obtained the best-fit model for a mixture of 80% porous RFA particles and 20% Solids that have a power-law size distribution index $n = 2.7$ using the parameterization scheme of Model_X and $n = 2.6$ using the parameterization scheme of Model_R for C:Si = 50:50 and wavelength filters $\lambda = 0.557 \mu\text{m}$ (V_f filter), $0.655 \mu\text{m}$ (R_f

filter), and $0.768 \mu\text{m}$ (I_f filter). The higher percentage of porous RFA structures and the higher power-law index indicate that the coma of 2I/Borisov is dominated by porous and relatively smaller dust particles. On the other hand, best-fit model results for short-period comets 1P/Halley, 67P/Churyumov-Gerasimenko, and 156P/Russel-LINEAR (Halder & Ganesh 2021; Aravind et al. 2022) indicate the presence of a lesser amount of porous aggregates. Also, the study indicates that the porous-to-compact ratio of dust particles is directly proportional to the dust-to-gas ratio observed in the coma of a comet. In the case of newer comets, the coma is dominated by a large number of small porous dust aggregates of Rayleigh-size grains, indicating a high dust-to-gas ratio owing to a high porous-to-compact ratio, thereby producing higher polarization. On the other hand, in the case of short-period or older comets, the coma is dominated by gas and large compact dust particles that are mainly concentrated in the inner coma and the near-nucleus regions, indicating low dust-to-gas ratio owing to a low porous-to-compact ratio, which in turn produces lower polarization. Thus, it is very clear from this study that dynamically new comets carry a larger number of porous pristine cosmic dust particles, while in dynamically older comets or short-period comets a larger portion of the pristine dust particles are lost due to frequent weathering by the solar wind. In this study we employ a multidimensional approach by considering morphologically realistic dust particles that have a mixture of high and low porosity over a wide range of sizes for the three broadband filters. We all know 2I/Borisov as an interstellar comet, yet it

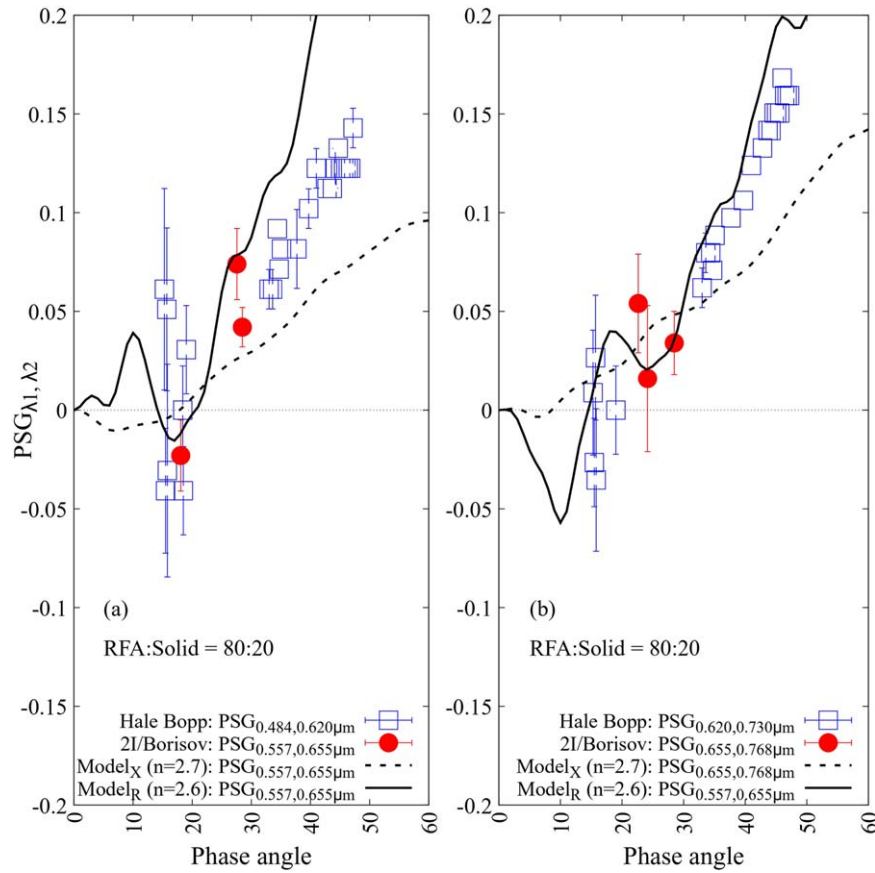


Figure 10. Best-fit results of polarimetric spectral gradient for the two pairs of wavelengths (a) $PSG_{0.557, 0.655}$ and (b) $PSG_{0.655, 0.768}$ using $Model_X$ (dashed line) and $Model_R$ (solid line) over the observed PSG values for Hale-Bopp (blue hollow square) and 2I/Borisov (red solid circle).

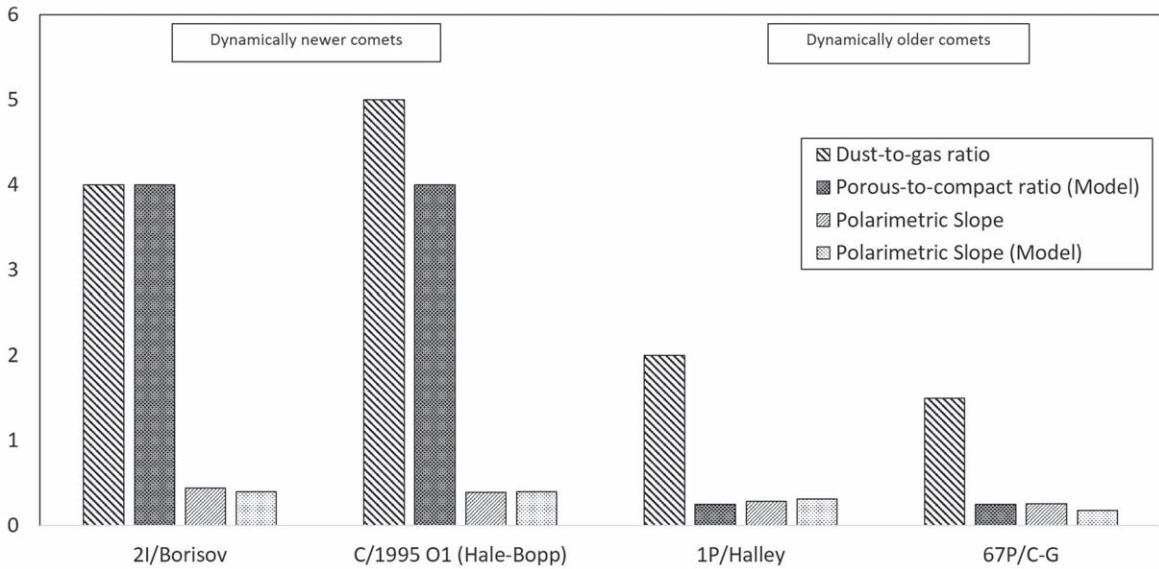


Figure 11. Comparison of dust-to-gas ratio (measured; McDonnell et al. 1991; Jewitt et al. 1999; Biver et al. 2019; Yang et al. 2021), porous-to-compact ratio (modeled), and polarimetric slope (observed and modeled) for dynamically newer and older comets.

was once part of an extrasolar planetary system and hence it was an exocomet before drifting away from its host star. Astronomers have recently found signatures of exocomets using techniques such as photometric transits and far-IR/millimeter gas emission from within debris disks (Ström et al. 2020; Lecavelier des Etangs et al. 2022). On the other hand,

recent observations of main-belt comets (active asteroids) reveal a certain amount of dust and gas production (Jewitt 2012; Moreno et al. 2021). Hence, the correlation between dust-to-gas ratio and porous-to-compact ratio indicated in this study can be of great use to determine the intrinsic dust properties in main-belt comets and exocomets. The model has been verified

considering best-fit results for the observed polarization and polarimetric spectral gradient of the interstellar comet 2I/Borisov. This study ensures that the RFA model structures represent the pristine morphology of cosmic dust particles and are capable of reproducing experimental as well as observational data. Hence, these structures will be highly useful for future studies related to cometary dust polarization, polarimetric response from protoplanetary disks, atmospheres of cloudy exoplanets and brown dwarfs (Sengupta & Krishan 2001; Marley & Sengupta 2011; Chakrabarty et al. 2022), extinction of background starlight in dense molecular clouds, and polarimetric study of dust in circumstellar environments. Although we tried to develop a realistic cosmic dust model considering realistic dust particles that have surface roughness/irregularities, the model can be improved by considering large hierarchical aggregates and including compositions such as organics, FeS, and different kinds of ices. These limitations can be addressed in some future work to develop a more realistic and generalized model of comet dust.

The authors deeply thank the anonymous reviewers for their fruitful suggestions, which have enriched the manuscript with

greater details. The authors acknowledge the high-performance computing facility (NOVA) of the Indian Institute of Astrophysics, Bangalore, where all the intensive light scattering simulations are conducted. The authors also acknowledge Prof. Shashikiran Ganesh of PRL, Ahmedabad and Dr. Himadri Sekhar Das of Dept. of Physics, Assam University, Silchar for important discussions.

Appendix RFA Model Structures

The RFA model structures used in this study are the exact computer-modeled replica of circumstellar dust analogs prepared in the Amsterdam Granada Light Scattering setup. Figure 12 depicts the RFA model realizations of circumstellar dust analog samples (1–6) that have similar refractive index (n), porosity, grain size, and aggregate size following Table 3 of Volten et al. (2007). The different physical parameters of the RFA model structures are shown in Table 5. For simplicity we considered the imaginary part of the refractive index $k = 0.0001$ for all the structures, as it was not detected in the experiments.

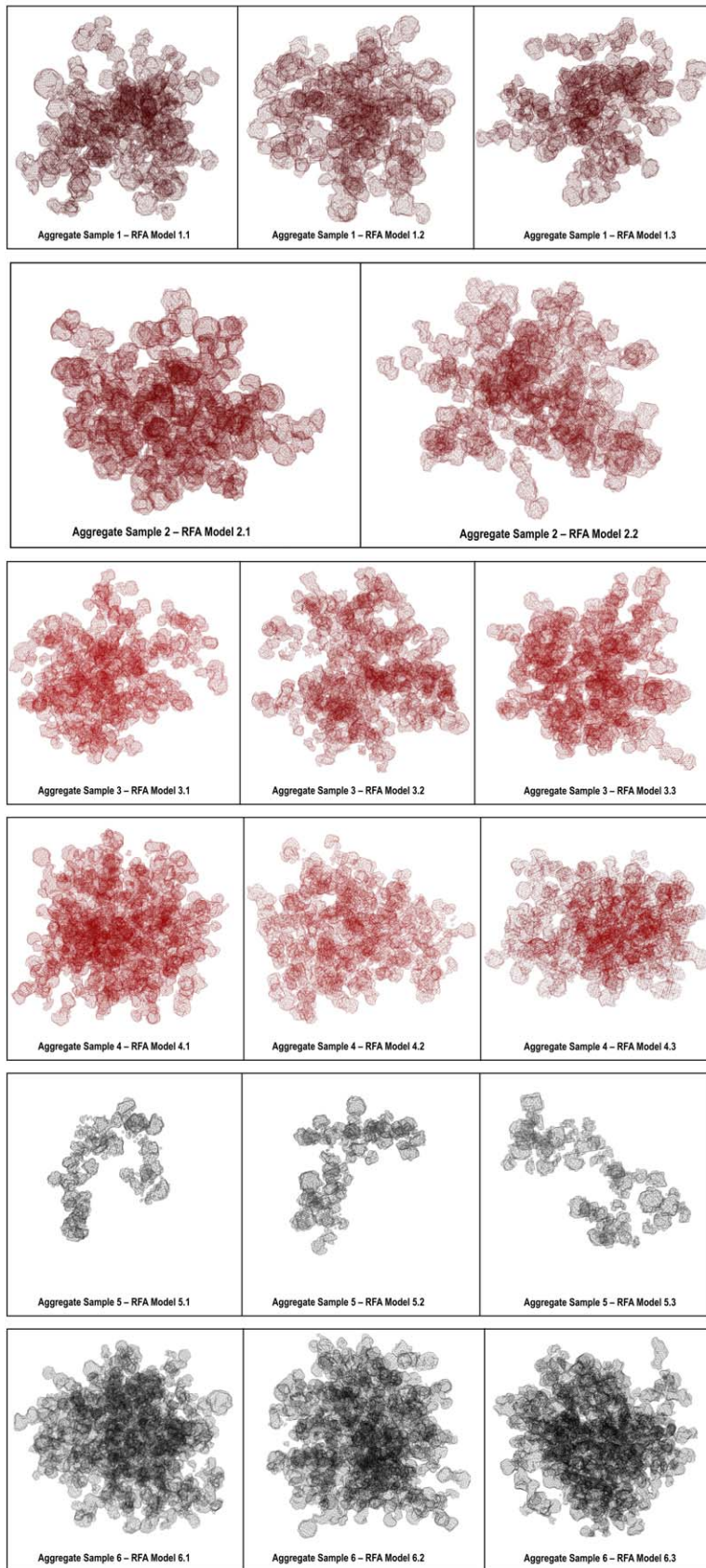


Figure 12. RFA model structures (1–6) representing aggregate samples (1–6) from the Granada Amsterdam Light Scattering Database.

ORCID iDs

Prithish Halder  <https://orcid.org/0000-0002-1073-1419>
 Sujan Sengupta  <https://orcid.org/0000-0002-6176-3816>

References

- A'Hearn, M. F., Belton, M. J. S., Delamere, W. A., et al. 2011, *Sci*, **332**, 1396
 A'Hearn, M. F., Millis, R. C., Schleicher, D. G., Osip, D. J., & Birch, P. V. 1995, *Icar*, **118**, 223
 Aravind, K., Ganesh, S., Venkataramani, K., et al. 2021, *MNRAS*, **502**, 3491
 Aravind, K., Halder, P., Ganesh, S., et al. 2022, *Icar*, **383**, 115042
 Bagnulo, S., Cellino, A., Kolokolova, L., et al. 2021, *NatCo*, **12**, 1797
 Bardin, A., Baklouti, D., Cottin, H., et al. 2017, *MNRAS*, **469**, S712
 Bentley, M. S., Schmied, R., Mannel, T., et al. 2016, *Natur*, **537**, 73
 Biver, N., Bockelée-Morvan, D., Hofstadter, M., et al. 2019, *A&A*, **630**, A19
 Blum, J., & Wurm, G. 2000, *Icar*, **143**, 138
 Bohren, C. F., & Huffman, D. R. 1998, *Absorption and Scattering of Light by Small Particles* (Weinheim: Wiley-VCH)
 Brownlee, D. E. 2003, *AREPS*, **13**, 147
 Chakrabarty, A., Sengupta, S., & Marley, M. S. 2022, *ApJ*, **927**, 51
 Chernova, G. P., Kiselev, N. N., & Jockers, K. 1993, *Icar*, **103**, 144
 Das, H. S., Das, S. R., & Sen, A. K. 2008, *MNRAS*, **390**, 1195
 Deb Roy, P., Halder, P., & Das, H. 2017, *Ap&SS*, **362**, 209
 Draine, B. T., & Flatau, P. J. 1994, *JOSAA*, **11**, 1491
 Eggersdorfer, M. L., & Pratsinis, S. E. 2011, *AerSE*, **46**, 347
 Ganesh, S., Joshi, U. C., Baliyan, K. S., & Deshpande, M. R. 1998, *A&AS*, **129**, 489
 Güttler, C., Mannel, T., Rotundi, A., et al. 2019, *A&A*, **630**, A24
 Hadamcik, E., & Levasseur-Regourd, A. C. 2003, *JQSRT*, **79-80**, 661
 Halder, P. 2022, *ApJS*, **263**, 3
 Halder, P., Deb Roy, P., & Das, H. S. 2018, *Icar*, **312**, 45
 Halder, P., & Ganesh, S. 2021, *MNRAS*, **501**, 1766
 Jenniskens, P., & Jenniskens, P. 1993, *A&A*, **274**, 653
 Jewitt, D. 2012, *AJ*, **143**, 66
 Jewitt, D., Matthews, H., Jewitt, D., & Matthews, H. 1999, *AJ*, **117**, 1056
 Kikuchi, S. 2006, *JQSRT*, **100**, 179
 Kimura, H., Kolokolova, L., & Mann, I. 2006, *A&A*, **449**, 1243
 Kolokolova, L., Das, H. S., Dubovik, O., Lapyonok, T., & Yang, P. 2015, *P&SS*, **116**, 30
 Krause, M., & Blum, J. 2004, *PhRvL*, **93**, 021103
 Lasue, J., Levasseur-regourd, A., Hadamcik, E., & Alcouffe, G. 2009, *Icar*, **199**, 129
 Lasue, J., & Levasseur-Regourd, A. C. 2006, *JQSRT*, **100**, 220
 Lecavelier des Etangs, A., Cros, L., Hébrard, G., et al. 2022, *NatSR*, **12**, 5855
 Levasseur-Regourd, A. C., Hadamcik, E., & Renard, J. B. 1996, *A&A*, **313**, 327
 Li, A., Greenberg, J. M., Li, A., & Greenberg, J. M. 1997, *A&A*, **323**, 566
 Mannel, T., Bentley, M. S., Boakes, P. D., et al. 2019, *A&A*, **630**, A26
 Markkanen, J., Penttilä, A., Peltoniemi, J., & Muinonen, K. 2015, *P&SS*, **118**, 164
 Marley, M. S., & Sengupta, S. 2011, *MNRAS*, **417**, 2874
 McDonnell, J. A. M., Lamy, P. L., & Pankiewicz, G. S. 1991, *IAU Colloq.*, **116**, 1043
 Moreno, F., Licandro, J., Cabrera-Lavers, A., Morate, D., & Guirado, D. 2021, *MNRAS*, **506**, 1733
 Muinonen, K., Nousiainen, T., Fast, P., Lumme, K., & Peltoniemi, J. I. 1996, *JQSRT*, **55**, 577
 Noguchi, T., Ohashi, N., Tsujimoto, S., et al. 2015, *E&PSL*, **410**, 1
 Nuth, J. A., Hallenbeck, S. L., & Rietmeijer, F. J. M. 2000, *JGRA*, **105**, 10387
 Rietmeijer, F. J. M., Nuth, J. A., I, Karner, J. M., et al. 1999, *ApJ*, **527**, 395
 Schulz, R., Hilchenbach, M., Langevin, Y., et al. 2015, *Natur*, **518**, 216
 Scott, A., Duley, W. W., Scott, A., & Duley, W. W. 1996, *ApJS*, **105**, 401
 Sen, A., & Rana, N. 1993, *A&A*, **275**, 298
 Sengupta, S., & Krishan, V. 2001, *ApJ*, **561**, 123
 Skorupski, K., Mroczka, J., Wriedt, T., & Riefler, N. 2014, *PhyA*, **404**, 106
 Sorensen, C. M., Cai, J., & Lu, N. 1992, *ApOpt*, **31**, 6547
 Strøm, P. A., Bodewits, D., Knight, M. M., et al. 2020, *PASP*, **132**, 101001
 Volten, H., Muñoz, O., Hovenier, J. W., et al. 2007, *A&A*, **470**, 377
 Wurm, G., & Blum, J. 1998, *Icar*, **132**, 125
 Yang, B., Li, A., Cordiner, M. A., et al. 2021, *NatAs*, **5**, 586
 Zubko, E., Shkuratov, Y., Kiselev, N. N., & Videen, G. 2006, *JQSRT*, **101**, 416
 Zubko, E., Videen, G., Arnold, J. A., et al. 2020, *ApJ*, **895**, 110